

Modeling of Joint Parker Solar Probe–Metis/Solar Orbiter Observations

L. Adhikari¹ , G. P. Zank¹ , D. Telloni² , and L.-L. Zhao¹ 

¹ Center for Space Plasma and Aeronomics Research (CSPAR), and Department of Space Science, University of Alabama in Huntsville, Huntsville, AL 35899, USA
la0004@uah.edu

² National Institute for Astrophysics—Astrophysical Observatory of Torino Via Osservatorio 20, I-10025 Pino Torinese, Italy

Received 2022 May 14; revised 2022 September 2; accepted 2022 September 13; published 2022 September 27

Abstract

We present the first theoretical modeling of joint Parker Solar Probe (PSP)–Metis/Solar Orbiter (SolO) quadrature observations. The combined observations describe the evolution of a slow solar wind plasma parcel from the extended solar corona (3.5 – $6.3 R_{\odot}$) to the very inner heliosphere ($23.2 R_{\odot}$). The Metis/SolO instrument remotely measures the solar wind speed finding a range from 96 to 201 km s^{-1} , and PSP measures the solar wind plasma *in situ*, observing a radial speed of 219.34 km s^{-1} . We find theoretically and observationally that the solar wind speed accelerates rapidly within 3.3 – $4 R_{\odot}$ and then increases more gradually with distance. Similarly, we find that the theoretical solar wind density is consistent with the remotely and *in-situ* observed solar wind density. The normalized cross helicity and normalized residual energy observed by PSP are 0.96 and -0.07 , respectively, indicating that the slow solar wind is very Alfvénic. The theoretical NI/slab results are very similar to PSP measurements, which is a consequence of the highly magnetic field-aligned radial flow ensuring that PSP can measure slab fluctuations and not 2D ones. Finally, we calculate the theoretical 2D and slab turbulence pressure, finding that the theoretical slab pressure is very similar to that observed by PSP.

Unified Astronomy Thesaurus concepts: [The Sun \(1693\)](#); [Solar wind \(1534\)](#); [Interplanetary turbulence \(830\)](#)

1. Introduction

One of the main purposes of the Parker Solar Probe (PSP) and Solar Orbiter (SolO) is to understand coronal heating, and the acceleration of the solar wind. Turbulence is thought to be a central element in addressing these questions. PSP and SolO allow us to study the radial evolution of turbulence in the inner heliosphere (e.g., Telloni et al. 2021; Adhikari et al. 2022; Telloni et al. 2022b). Adhikari et al. (2022) studied the evolution of 2D and slab turbulence in similar types of slow solar wind observed by PSP (Bale et al. 2016; Kasper et al. 2016) and SolO (Horbury et al. 2020; Owen et al. 2020), finding that 2D turbulence is the dominant component. Telloni et al. (2021) studied the evolution of turbulence in the same plasma parcel measured by PSP and SolO, using a radial alignment between PSP and SolO from 0.1 au (PSP’s position) to 1 au (SolO’s position). This alignment facilitates the study of turbulence characteristics on the same plasma parcel with different locations.

When PSP was at 0.11 au on 2021 January 18 at 18:59 UT during encounter 7, PSP entered the plane of sky (POS) measured by the SolO coronagraph Metis on 2021 January 17 at 16:30 UT (Telloni et al. 2022b; interval #1). Five days later, when PSP was at 0.26 au on 2021 January 23 at 17:02 UT, PSP again crossed the POS corresponding to the longitude observed by Metis (Telloni et al. 2022b; interval #2). Telloni et al. (2022b) presented the first observational study that combined *in-situ* PSP data and remote Metis/SolO observations. Their unique configuration allowed Telloni et al. to follow the evolution of a plasma parcel through the extended solar corona (3.5 – $6.3 R_{\odot}$, where $R_{\odot} = 6.95 \times 10^5 \text{ km}$) to the very inner heliosphere. Telloni et al. (2022b) therefore provide plasma observations from the sub-Alfvénic corona to the super-Alfvénic solar wind.

Using a potential field source surface (PFSS) extrapolation (e.g., Panasenco et al. 2020), Telloni et al. (2022b) found that PSP sampled plasma coming from the equatorial extension of the southern polar coronal hole (interval #1) and plasma coming from the low latitude of a northern coronal hole (interval #2). During interval #1, PSP observed almost exclusively outwardly propagating Alfvén waves ($\sigma_c \sim 1$, where σ_c is the normalized cross helicity), whereas interval #2 contains switchbacks (Bale et al. 2019; Telloni et al. 2022b). In this letter, we model the solar wind plasma (interval #1) measured by the PSP—SolO quadrature from the sub- to super-Alfvénic solar wind and compare the predicted solar wind radial profile with the combined PSP (*in situ*)—Metis (remote data set). Our model describes the (coronal) heating of the slow solar wind and the acceleration of the solar wind near the equatorial region (Fisk 2003; Telloni et al. 2022b). The origin of the slow solar wind is thought to be due to the interchange reconnection between the open and closed magnetic field lines near equatorial regions at a height of about 2 – $5 R_{\odot}$ above the solar surface (Fisk 2003; Zank et al. 2021). However, fast solar wind emerges from coronal holes in polar regions (Matthaeus et al. 1999; Dmitruk et al. 2001; Chandran & Hollweg 2009; Cranmer & van Ballegooijen 2010; Verdini et al. 2010; Cranmer et al. 2013; Zank et al. 2018a; Adhikari et al. 2020). Although, the physical origin of the fast and slow solar wind is different, Zank et al. (2021) argued that plasma in both open and closed/loop regions is heated via the same turbulence-associated mechanism.

We structure the letter as follows. Section 2 discusses a solar wind model that incorporates nearly incompressible (NI) magnetohydrodynamic (MHD) turbulence. Section 3 discusses the data analysis. Section 4 compares the theoretical and observed results. Finally, Section 5 presents the conclusions.

2. A Turbulent Solar Wind Model

In the letter, we use a superradial expansion turbulence-driven solar model (Telloni et al. 2022a) to study the coronal plasma in the slow solar wind that the hot plasma emerges from



Original content from this work may be used under the terms of the [Creative Commons Attribution 4.0 licence](#). Any further distribution of this work must maintain attribution to the author(s) and the title of the work, journal citation and DOI.

the closed loop into the open field region by interchange reconnection, after which it expands superradially. We consider a steady flow in a one-dimensional, superradially expanding the open flux tube of the cross-sectional area $A(r) = r^2 f(r)$ (where $f(r)$ is a superradial expansion factor), which is inversely proportional to the magnetic field strength $B(r)$,

$$B_r A(r) = B_r r^2 f(r) = \text{const.} \quad (1)$$

The superradial expansion term $f(r)$ is given by Kopp & Holzer (1976),

$$f(r) = \frac{f_m \exp\left(\frac{r-r_a}{\sigma}\right) + 1 - (f_m - 1)\exp\left(\frac{R_\odot - r_a}{\sigma}\right)}{\exp\left(\frac{r-r_a}{\sigma}\right) + 1}, \quad (2)$$

where $f_m = 2$, $r_a = 2 R_\odot$, and $\sigma = 0.8 R_\odot$. The steady flow in the superradially expanding tube can be described by the continuity, inviscid momentum, and pressure equations,

$$\begin{aligned} \frac{dn_s}{dr} &= -\frac{2n_s}{r} - \frac{n_s}{U} \frac{dU}{dr} \\ &\quad - \frac{n_s}{\sigma f(r)} \exp\left(\frac{r-r_a}{\sigma}\right) \frac{f_m - f(r)}{\exp\left(\frac{r-r_a}{\sigma}\right) + 1}; \end{aligned} \quad (3)$$

$$\rho U \frac{dU}{dr} = -\frac{dP}{dr} - \frac{GM_\odot}{r^2} \rho; \quad (4)$$

$$\begin{aligned} \frac{dP}{dr} &= -\frac{\gamma P}{U} \frac{dU}{dr} - \frac{2\gamma P}{r} \\ &\quad - \frac{\gamma P}{\sigma f(r)} \exp\left(\frac{r-r_a}{\sigma}\right) \frac{f_m - f(r)}{\exp\left(\frac{r-r_a}{\sigma}\right) + 1} + (\gamma - 1) s_1 \frac{S_t}{U}, \end{aligned} \quad (5)$$

where $n_s(\rho)$ is the solar wind (mass) density, U is the solar wind speed, P is the thermal pressure, G is the gravitational constant, M_\odot is the solar mass, S_t is the turbulent heating term, and $\gamma = 5/3$ is the polytropic index. Parameter s_1 denotes the fraction of turbulence energy used to heat the coronal plasma (protons). We use $s_1 = 0.6$, meaning that the 60% of the turbulent energy heats the coronal/solar wind (proton) plasma (Breech et al. 2009; Cranmer et al. 2009; Engelbrecht & Strauss 2018; Chhiber et al. 2019; Adhikari et al. 2021b; Telloni et al. 2022a). Combining the above equations yields

$$\begin{aligned} \frac{C_s^2}{U^2} (M_s^2 - 1) \frac{dU}{dr} &= \frac{2\gamma P}{\rho Ur} - (\gamma - 1) s_1 \alpha \frac{S_t}{m_p n_s U^2} \\ &\quad - \frac{GM_\odot}{Ur^2} + \frac{\gamma P}{\sigma f(r) \rho U} \exp\left(\frac{r-r_a}{\sigma}\right) \frac{f_m - f(r)}{\exp\left(\frac{r-r_a}{\sigma}\right) + 1}, \end{aligned} \quad (6)$$

where $M_s = U/C_s$ is the sonic Mach number, and $C_s^2 = \gamma P/\rho$ is the square of the sound speed. Equation (6) possesses a critical point, where $M_s = 1$ and the right-hand side (rhs) is zero simultaneously. We use L'Hôpital's rule to solve Equation (6) in the vicinity of the critical point. This solar wind model (Equations (3)–(5)) includes only the thermal force and not the ponderomotive force (see Holzer & Axford 1970; Leer et al. 1982; Withbroe 1988; Fisk et al. 1999; Cranmer & van Ballegooijen 2010; Verdini et al. 2010; Cranmer et al. 2013) or wave pressure (McKenzie et al. 1995). As the particle pressure is larger than the ponderomotive force, the ponderomotive force can

be neglected because the radial magnetic field does not exert a direct force on the mean flow (Fisk et al. 1999). Equations (3)–(6) can be reduced to Equations (2)–(5) of Adhikari et al. (2020) in the absence of the superradial expansion term.

The turbulent heating term S_t can be derived from a von Kármán phenomenology (von Karman & Howarth 1938). The heating term of the magnetized solar wind plasma can be written as (Verdini et al. 2010; Wan et al. 2012; Adhikari et al. 2015; Zank et al. 2018b)

$$S_t = \alpha m_p n_s \left[2 \frac{\langle z^{\infty+2} \rangle^2 \langle z^{\infty-2} \rangle^{1/2}}{L_\infty^+} + 2 \frac{\langle z^{\infty-2} \rangle^2 \langle z^{\infty+2} \rangle^{1/2}}{L_\infty^-} + 2 \frac{\langle z^{*+2} \rangle \langle z^{\infty+2} \rangle \langle z^{\infty-2} \rangle^{1/2}}{L_\infty^+} \right], \quad (7)$$

where $\alpha(=0.01)$ is a von Kármán–Taylor constant, and m_p is the proton mass. The first, second, and third terms inside [...] correspond to the dissipation terms of the 2D outward Elsässer energy $\langle z^{\infty+2} \rangle$ (the fifth term on the rhs of Equation (8)), the 2D inward Elsässer energy $\langle z^{\infty-2} \rangle$ (the fifth term on the rhs of Equation (9)), and the NI/slab outward Elsässer energy $\langle z^{*+2} \rangle$ (the fifth term on the rhs of Equation (16)), respectively. The dimension of each term inside [...] is (speed)³/length. Parameter $L_\infty^\pm (\equiv \langle z^{\infty\pm 2} \rangle \lambda_\infty^\pm)$, where λ_∞^\pm is the correlation length corresponding to the 2D outward/inward Elsässer energy) is the energy-weighted correlation length corresponding to the 2D outward/inward Elsässer energy.

Equation (7) couples the solar wind equations and the turbulence transport model equations. The 1D steady-state transport equations for the majority 2D turbulence, including the superradial expansion factor are given by Zank et al. (2017), Adhikari et al. (2020), and Telloni et al. (2022a)

$$\begin{aligned} U \frac{d\langle z^{\infty\pm 2} \rangle}{dr} &= -\left(\frac{\langle z^{\infty\pm 2} \rangle}{2} + \left(2a - \frac{1}{2}\right) E_D^\infty \right) \\ &\quad \times \frac{dU}{dr} - \frac{2U}{r} \left(\frac{\langle z^{\infty\pm 2} \rangle}{2} + \left(2a - \frac{1}{2}\right) E_D^\infty \right) \\ &\quad - \frac{U}{\sigma f(r)} \left(\frac{\langle z^{\infty\pm 2} \rangle}{2} + \left(2a - \frac{1}{2}\right) E_D^\infty \right) \\ &\quad \times \exp\left(\frac{r-r_a}{\sigma}\right) \frac{f_m - f(r)}{\exp\left(\frac{r-r_a}{\sigma}\right) + 1} \\ &\quad - 2\alpha \frac{\langle z^{\infty\pm 2} \rangle^2 \langle z^{\infty\mp 2} \rangle^{1/2}}{L_\infty^\pm} + S^{\langle z^{\infty\pm 2} \rangle}; \end{aligned} \quad (8)$$

$$\begin{aligned} U \frac{dE_D^\infty}{dr} &= -\left(\frac{E_D^\infty}{2} + \left(2a - \frac{1}{2}\right) E_T^\infty \right) \\ &\quad \times \frac{dU}{dr} - \frac{2U}{r} \left(\frac{E_D^\infty}{2} + \left(2a - \frac{1}{2}\right) E_T^\infty \right) \\ &\quad - \frac{U}{\sigma f(r)} \left(\frac{E_D^\infty}{2} + \left(2a - \frac{1}{2}\right) E_T^\infty \right) \\ &\quad \times \exp\left(\frac{r-r_a}{\sigma}\right) \frac{f_m - f(r)}{\exp\left(\frac{r-r_a}{\sigma}\right) + 1} \\ &\quad - \alpha E_D^\infty \left(\frac{\langle z^{\infty+2} \rangle^{1/2} \langle z^{\infty-2} \rangle}{L_\infty^-} + \frac{\langle z^{\infty-2} \rangle^{1/2} \langle z^{\infty+2} \rangle}{L_\infty^+} \right) \\ &\quad + S^{E_D^\infty}; \end{aligned} \quad (9)$$

$$\begin{aligned}
U \frac{dL_D^\pm}{dr} = & - \left(\frac{L_D^\pm}{2} + \left(a - \frac{1}{4} \right) L_D^\infty \right) \frac{dU}{dr} - \frac{2U}{r} \\
& \times \left(\frac{L_D^\pm}{2} + \left(a - \frac{1}{4} \right) L_D^\infty \right) \\
& - \frac{U}{\sigma f(r)} \left(\frac{L_D^\pm}{2} + \left(a - \frac{1}{4} \right) L_D^\infty \right) \\
& \times \exp \left(\frac{r - r_a}{\sigma} \right) \frac{f_m - f(r)}{\exp \left(\frac{r - r_a}{\sigma} \right) + 1}; \quad (10)
\end{aligned}$$

$$\begin{aligned}
U \frac{dL_D^\infty}{dr} = & - \left(\frac{L_D^\infty}{2} + \left(2a - \frac{1}{2} \right) (L_\infty^+ + L_\infty^-) \right) \frac{dU}{dr} \\
& - \frac{2U}{r} \left(\frac{L_D^\infty}{2} + \left(2a - \frac{1}{2} \right) (L_\infty^+ + L_\infty^-) \right) - \frac{U}{\sigma f(r)} \\
& \times \left(\frac{L_D^\infty}{2} + \left(2a - \frac{1}{2} \right) (L_\infty^+ + L_\infty^-) \right) \\
& \times \exp \left(\frac{r - r_a}{\sigma} \right) \frac{f_m - f(r)}{\exp \left(\frac{r - r_a}{\sigma} \right) + 1}, \quad (11)
\end{aligned}$$

where $L_D^\infty (\equiv E_D^\infty \lambda_D^\infty)$, where λ_D^∞ is the correlation length of the 2D residual energy) is the energy-weighted correlation length for the 2D residual energy E_D^∞ , and E_T^∞ is the 2D total turbulence energy. In the absence of the superradial expansion term, Equations (8)–(11) reduce to the Equations (8)–(11) of Adhikari et al. (2020). The term “S” refers to the turbulent shear source for the 2D outward and inward Elsässer energies and the residual energy. From the addition and subtraction of Equations (8), the transport equation for $E_T^\infty = (\langle z^{\infty+2} \rangle + \langle z^{\infty-2} \rangle)/2$ and cross helicity $E_C^\infty = (\langle z^{\infty+2} \rangle - \langle z^{\infty-2} \rangle)/2$ can be derived as,

$$\begin{aligned}
U \frac{dE_T^\infty}{dr} = & - \left(\frac{E_T^\infty}{2} + \left(2a - \frac{1}{2} \right) E_D^\infty \right) \frac{dU}{dr} \\
& - \frac{2U}{r} \left(\frac{E_T^\infty}{2} + \left(2a - \frac{1}{2} \right) E_D^\infty \right) - \frac{U}{\sigma f(r)} \\
& \times \left(\frac{E_T^\infty}{2} + \left(2a - \frac{1}{2} \right) E_D^\infty \right) \exp \left(\frac{r - r_a}{\sigma} \right) \\
& \times \frac{f_m - f(r)}{\exp \left(\frac{r - r_a}{\sigma} \right) + 1} \\
& - \alpha \frac{|E_T^\infty + E_C^\infty|^2 |E_T^\infty - E_C^\infty|^{1/2}}{L_\infty^+} \\
& - \alpha \frac{|E_T^\infty - E_C^\infty|^2 |E_T^\infty + E_C^\infty|^{1/2}}{L_\infty^+} \\
& + \frac{S^{\langle z^{\infty+2} \rangle} + S^{\langle z^{\infty-2} \rangle}}{2}; \quad (12)
\end{aligned}$$

$$\begin{aligned}
U \frac{dE_C^\infty}{dr} = & - \frac{E_C^\infty}{2} \frac{dU}{dr} - \frac{U}{r} E_C^\infty \\
& - \frac{U}{2\sigma f(r)} E_C^\infty \exp \left(\frac{r - r_a}{\sigma} \right) \frac{f_m - f(r)}{\exp \left(\frac{r - r_a}{\sigma} \right) + 1} \\
& - \alpha \frac{|E_T^\infty + E_C^\infty|^2 |E_T^\infty - E_C^\infty|^{1/2}}{L_\infty^+} \\
& + \alpha \frac{|E_T^\infty - E_C^\infty|^2 |E_T^\infty + E_C^\infty|^{1/2}}{L_\infty^+} \\
& + \frac{S^{\langle z^{\infty+2} \rangle} - S^{\langle z^{\infty-2} \rangle}}{2}, \quad (13)
\end{aligned}$$

where the fourth and fifth terms on the rhs of both equations denote the nonlinear terms, and the sixth term denotes the turbulent source. Similarly, Equation (12) can be written in the conservation form as (Wang et al. 2022),

$$\begin{aligned}
& \frac{1}{r^2 f(r)} \frac{d}{dr} [r^2 f(r) U (E_w^\infty + P_w^\infty)] \\
& = U \frac{dP_w^\infty}{dr} + \rho \left[- \alpha \frac{|E_T^\infty + E_C^\infty|^2 |E_T^\infty - E_C^\infty|^{1/2}}{L_\infty^+} \right. \\
& \left. - \alpha \frac{|E_T^\infty - E_C^\infty|^2 |E_T^\infty + E_C^\infty|^{1/2}}{L_\infty^+} + \frac{S^{\langle z^{\infty+2} \rangle} + S^{\langle z^{\infty-2} \rangle}}{2} \right], \quad (14)
\end{aligned}$$

where $E_w^\infty = \rho E_T^\infty / 2$ is the 2D turbulence energy density, and

$$\begin{aligned}
P_w^\infty = & \frac{\rho}{2} \left[\frac{E_T^\infty}{2} + \left(2a - \frac{1}{2} \right) E_D^\infty \right] \\
& = \frac{E_w^\infty}{2} \left[1 + 2 \left(2a - \frac{1}{2} \right) \sigma_D^\infty \right] \quad (15)
\end{aligned}$$

is the 2D turbulence pressure. In the absence of the nonlinear term and turbulence source terms, Equation (14) resembles the well-known Wentze–Kramers–Brillouin (WKB) form. The terms in the square bracket on the left-hand side (lhs) of Equation (14) express the energy density flux vector, which describes the amount of turbulence energy per unit time per unit area in a direction perpendicular to the velocity (Landau & Lifshitz 1987). Similarly, on the lhs, the first term in [...] describes the energy transmitted through the unit surface area per unit time, and the second term describes the work done by the turbulence pressure on the plasma on the surface. The first term on the rhs describes the rate of turbulence pressure gradient on the background plasma flow.

The 1D steady-state transport equations for the energy in NI/slab forward-propagating modes and the corresponding energy-weighted correlation length are (Zank et al. 2017;

Adhikari et al. 2020; Telloni et al. 2022a),

$$(U - V_A) \frac{d \langle z^{*+2} \rangle}{dr} = -\frac{1}{2} \frac{dU}{dr} \langle z^{*+2} \rangle + (2b - 1) \frac{U}{r} \langle z^{*+2} \rangle + \frac{V_A}{2\rho} \frac{d\rho}{dr} \langle z^{*+2} \rangle + \frac{1}{2} (2b - 1) \frac{U \langle z^{*+2} \rangle}{\sigma f(r)} \times \exp\left(\frac{r - r_a}{\sigma}\right) \frac{f_m - f(r)}{\exp\left(\frac{r - r_a}{\sigma}\right) + 1} - 2\alpha \frac{\langle z^{*+2} \rangle \langle z^{\infty+2} \rangle \langle z^{\infty-2} \rangle^{1/2}}{L_{\infty}^+} + S^{\langle z^{*+2} \rangle}; \quad (16)$$

$$(U - V_A) \frac{dL_*^+}{dr} = -\frac{1}{2} \frac{dU}{dr} L_*^+ + (2b - 1) \frac{U}{r} L_*^+ + \frac{V_A}{2\rho} \frac{d\rho}{dr} L_*^+ + \frac{1}{2} (2b - 1) \frac{UL_*^+}{\sigma f(r)} \times \exp\left(\frac{r - r_a}{\sigma}\right) \frac{f_m - f(r)}{\exp\left(\frac{r - r_a}{\sigma}\right) + 1}. \quad (17)$$

Parameter $V_A (= (B_0 / \sqrt{\mu_0 \rho}) (r_0 / r)^2 (1/f(r)))$, where B_0 is the magnetic field at a reference point r_0 , and μ_0 is the magnetic permeability, is the large-scale Alfvén velocity. Parameter $S^{\langle z^{*+2} \rangle}$ denotes the turbulent shear source for the energy in NI/slab forward-propagating modes. The fifth term on the rhs of Equation (16) denotes the dissipation term. We use $b = 0.26$ (see Zank et al. 2012, 2017, for further discussion). Equation (16) can be written in terms of the slab total turbulent energy $E_T^* (= \langle z^{*+2} \rangle / 2 \equiv E_C^*, \langle z^{\infty-2} \rangle = 0)$ as

$$(U - V_A) \frac{dE_T^*}{dr} = -\frac{1}{2} \frac{dU}{dr} E_T^* + (2b - 1) \times \frac{U}{r} E_T^* + \frac{V_A}{2\rho} \frac{d\rho}{dr} E_T^* + \frac{1}{2} (2b - 1) \frac{U}{\sigma f(r)} E_T^* \times \exp\left(\frac{r - r_a}{\sigma}\right) \frac{f_m - f(r)}{\exp\left(\frac{r - r_a}{\sigma}\right) + 1} - 2\alpha \frac{E_T^* |E_T^{\infty} + E_C^{\infty}| |E_T^{\infty} - E_C^{\infty}|^{1/2}}{L_{\infty}^+} + \frac{S^{\langle z^{*+2} \rangle}}{2}, \quad (18)$$

where the fifth term on the rhs is the dissipation term, and the sixth term the turbulent source. Equation (18) can also be written in the conservation form as (Wang et al. 2022),

$$\begin{aligned} & \frac{1}{r^2 f(r)} \frac{d}{dr} [r^2 f(r) ((U - V_A) E_w^* + U P_w^*)] \\ &= U \frac{dP_w^*}{dr} + 2E_w^* \left(4b \frac{u}{r} + 2b \frac{U}{f(r)} \frac{df(r)}{dr} \right) \\ &+ \frac{\rho}{2} \left[-2\alpha \frac{E_T^* |E_T^{\infty} + E_C^{\infty}| |E_T^{\infty} - E_C^{\infty}|^{1/2}}{L_{\infty}^+} + \frac{S^{\langle z^{*+2} \rangle}}{2} \right], \end{aligned} \quad (19)$$

where $E_w^* = \rho E_T^* / 2$ is the slab turbulence energy density, and $P_w^* = E_w^* / 2$ is the slab turbulence pressure. Equation (19) also resembles the WKB form in the absence of the mixing term (the second term on the rhs), dissipation terms (the first term inside the square bracket [...] on the rhs), and the turbulence source term (the second term inside the square bracket [...] on the rhs).

Equations (8)–(13) and (16)–(18) are a set of non-WKB form of turbulence transport equations (Zhou & Matthaeus 1990c; Matthaeus et al. 1994), which describe the evolution of turbulence in highly field-aligned flows (see Adhikari et al. 2020, for a detailed discussion). Equations (16) and (17) are derived by considering unidirectional Alfvén waves, i.e., $u^* = b^* / \sqrt{\mu_0 \rho}$, where the slab velocity fluctuations u^* are perfectly aligned with the slab magnetic field fluctuations b^* normalized to the Alfvén unit $\sqrt{\mu_0 \rho}$, μ_0 is the magnetic permeability of free space, and ρ is the mean proton mass density.

Similar to Telloni et al. (2022a), we use two forms of the turbulent shear source: (i) in the region between the sonic surface and Alfvén surface, where the sound speed C_S is assumed to be the characteristic speed, and (ii) beyond the Alfvén surface, where the Alfvén speed is considered to be the characteristic speed. The shear source of turbulence in the region between the sonic and Alfvén surfaces can be written in the form (Telloni et al. 2022a)

$$\begin{aligned} S_{\langle z^{\infty,*\pm2} \rangle}^s &= C_{\infty,*}^{s+} \frac{r_0^s |\Delta U| C_s^2}{r^2} = \gamma C_{\infty,*}^{s+} \frac{r_0^s |U - U_0^{s'}| P}{\rho r^2}; \\ S_{\langle z^{\infty-2} \rangle}^s &= C_{\infty}^{s-} \frac{r_0^s |\Delta U| C_s^2}{r^2} = \gamma C_{\infty}^{s-} \frac{r_0^s |U - U_0^{s'}| P}{\rho r^2}; \\ S_{E_D^{\infty}}^s &= C_{\infty}^{sE_D} \frac{r_0^s |\Delta U| C_s^2}{r^2} = \gamma C_{\infty}^{sE_D} \frac{r_0^s |U - U_0^{s'}| P}{\rho r^2}, \end{aligned} \quad (20)$$

where $U_0^{s'}$ is the solar wind speed at r_0^s , a position above the sonic surface, and $C_{\infty,*}^{s\pm,E_D}$ denotes the strength of the shear source of turbulence. Here we use $\Delta U = |U - U_0^{s'}|$ and $C_s^2 = \gamma P / \rho$, which results in the shear source of turbulence depending on the distance r , the solar wind speed U , the thermal pressure P , and the proton mass density ρ . We use $r_0^s = 5.16 R_{\odot}$ and $U_0^{s'} = 173.5 \text{ km s}^{-1}$.

Similarly, the turbulent shear source above the Alfvén surface is,

$$\begin{aligned} S_{\langle z^{\infty,*\pm2} \rangle}^a &= C_{\infty,*}^{a+} \frac{r_0^a |\Delta U| V_A^2}{r^2} = C_{\infty,*}^{a+} \frac{r_0^a |U - U_0^{a'}| V_A^2}{r^2}; \\ S_{\langle z^{\infty-2} \rangle}^a &= C_{\infty}^{a-} \frac{r_0^a |\Delta U| V_{A0}^2}{r^2} = C_{\infty}^{a-} \frac{r_0^a |U - U_0^{a'}| V_A^2}{r^2}; \\ S_{E_D^{\infty}}^a &= C_{\infty}^{aE_D} \frac{r_0^a |\Delta U| V_{A0}^2}{r^2} = C_{\infty}^{aE_D} \frac{r_0^a |U - U_0^{a'}| V_A^2}{r^2}, \end{aligned} \quad (21)$$

where we use $\Delta U = |U - U_0^{a'}|$. Parameter $U_0^{a'}$ is the solar wind speed at r_0^a , a position above the Alfvén surface, and $C_{\infty,*}^{a\pm,E_D}$ denotes the strength of the shear source of turbulence. We use $r_0^a = 9.22 R_{\odot}$ and $U_0^{a'} = 222.87 \text{ km s}^{-1}$.

3. Data Analysis

We calculate the transverse turbulence energy and the transverse correlation length using a method developed by Adhikari et al. (2022). A fluctuating vector \mathbf{a} ($=a_r\hat{r} + a_t\hat{t} + a_n\hat{n}$, where a_r , a_t , a_n are the R , T , and N components of a vector \mathbf{a}) can be decomposed into parallel and perpendicular vectors relative to the mean magnetic field \mathbf{B} as

$$\mathbf{a} = \mathbf{a}_{\parallel} + \mathbf{a}_{\perp} = a_{\parallel}\hat{b} + \mathbf{a}_{\perp},$$

where $\hat{b} = \mathbf{B}/|\mathbf{B}|$ is the unit vector, $|\mathbf{B}|$ is the magnitude of the mean magnetic field \mathbf{B} ($=B_R\hat{r} + B_T\hat{t} + B_N\hat{n}$, where B_R , B_T , and B_N denote the R , T , and N components of the mean magnetic field), and \mathbf{a}_{\perp} and \mathbf{a}_{\parallel} ($=a_{\parallel}\hat{b}$) are the perpendicular and parallel vectors, respectively. The perpendicular vector \mathbf{a}_{\perp} can be derived as (Adhikari et al. 2022),

$$\begin{aligned} \mathbf{a}_{\perp} &= \frac{C_T B_N - C_N B_T}{B_R^2 + B_T^2 + B_N^2} \hat{r} + \frac{C_N B_R - C_R B_N}{B_R^2 + B_T^2 + B_N^2} \hat{t} \\ &+ \frac{C_R B_T - C_T B_R}{B_R^2 + B_T^2 + B_N^2} \hat{n}, \end{aligned} \quad (22)$$

where $C_R = B_T a_n - B_N a_t$, $C_T = B_N a_r - B_R a_n$, and $C_N = B_R a_t - B_T a_r$. Using Equation (22), we calculate the transverse Elsässer energies, fluctuating magnetic and kinetic energies, normalized cross helicity and residual energy, and the corresponding transverse correlation lengths.

4. Results

In this section, we compare the theoretical and observed results from the extended solar corona to the very inner heliosphere. We select SPAN ion plasma data (Kasper et al. 2016) and one-minute resolution FIELDS data (Bale et al. 2016) in the time interval 18:40–20:40 UT on 2021 January (interval #1) during E7. We apply a boxcar method to the SPAN ion data to remove large spikes, and smooth the data using one-minute long intervals, and then merge the plasma data with the magnetometer data. We calculate the transverse turbulence energy and the transverse correlation length, and the solar wind parameters for interval #1. The Metis/SolO plasma data (solar wind speed and density) are obtained from Telloni et al. (2022b). We use the Runge–Kutta fourth-order method to solve the solar wind + NI MHD turbulence transport equations from 3.3 to $30 R_{\odot}$. Table 1 shows the boundary conditions for the turbulence quantities and the solar wind parameters at $3.3 R_{\odot}$. Table 2 shows the values of the strength of the turbulent shear source. These boundary conditions are chosen so the theoretical results are close to the observations. We note that the theoretical results are similar with or without the turbulent shear source. In this letter, we include the turbulent shear source and compare the theoretical results with the observed results.

During the PSP—SolO Eastern-limb quadrature of mid-January, the same solar wind plasma stream was observed simultaneously in both the extended corona and the very inner heliosphere. The Metis coronagraph (Antonucci et al. 2020) on board SolO imaged the 3.5 – $6.3 R_{\odot}$ altitude range remotely, which corresponds to the coronal source region of the plasma flow impinging on PSP at 0.11 au (see Telloni et al. 2021, 2022b, for a detailed description of the orbital geometry and connectivity during quadrature). The Metis instrument is designed to observe

Table 1
Boundary Values at $3.3 R_{\odot}$ for the Turbulent Quantities and the Solar Wind Parameters

Parameters	Values
$\langle z^{\infty \pm 2} \rangle$ ($\text{km}^2 \text{s}^{-2}$)	10^5
E_D^{∞} ($\text{km}^2 \text{s}^{-2}$)	2000
L_{∞}^{\pm} ($\text{km}^3 \text{s}^{-2}$)	3.03×10^9
L_D^{∞} ($\text{km}^3 \text{s}^{-2}$)	1.6×10^8
$\langle z^{*+2} \rangle$ ($\text{km}^2 \text{s}^{-2}$)	6000
L_*^+ ($\text{km}^3 \text{s}^{-2}$)	9.1×10^7
U (km s^{-1})	45.13
n (cm^{-3})	8×10^5
T (K)	7×10^5

Table 2
Assumed Strengths for the Shear Driven Quasi-2D and Slab Turbulence in the Region between the Sonic and Alfvén Surfaces and above the Alfvén Surface

Parameters	Values
$C_{P\infty}^{s\pm}$	0.1
$C_{\infty}^{sE_D}$	-0.1
C_*^{s+}	0.1
$C_{\infty}^{a\pm}$	0.1
$C_{\infty}^{aE_D}$	-0.1
C_*^{a+}	0.1

the solar corona both in polarized brightness (pB) and H I Ly α ultraviolet (UV) emission. This allows for the study of complex coronal dynamics and structures. pB measurements are used to infer the electron density by exploiting the inversion technique developed by van de Hulst (1950). The UV light emitted by neutral hydrogen atoms is used as a proxy to estimate the outflow velocity of the proton component of the solar wind. The H I Ly α line emission at 121.6 nm is mainly due to resonant scattering processes of chromospheric radiation by coronal hydrogen atoms. It follows that an outward motion of the coronal plasma causes a reduction in intensity of the scattered Ly α line, as the incident radiation profile appears to be Doppler-shifted in the rest frame of the scattering atoms. This effect, known as Doppler dimming (Noci et al. 1987), can therefore be used to infer the expansion velocity of the coronal plasma. Based on a 3D model of the large-scale solar corona (involving prior knowledge of the electron density and temperature, kinetic temperature of scattering atoms, helium abundance, and temperature anisotropy, among others), the speed of the coronal flows is estimated by comparing the observed and synthesized H I Ly α line intensity (see Section 11.2 in Antonucci et al. 2020, for an exhaustive review of the Doppler dimming technique). Figure 1 displays the modeled plasma U and Alfvén V_A speed, and the proton number density, as a function of the altitude above the Sun. These profiles are compared with observations from SolO/Metis (open red triangles) and PSP (full triangles). Note that, accounting for a fully ionized plasma with 2.5% helium (according to Moses et al. 2020), the electron density estimates provided by Metis were multiplied by 0.95 to obtain the corresponding proton number density. The agreement between theory and observations is striking. The Metis and PSP measurements are obviously unrelated. One is obtained remotely and the other measured in situ. Evidently the model presented above reproduces very well the joint observations of the extended corona and the very inner heliosphere and the dynamic evolution of the solar wind plasma.

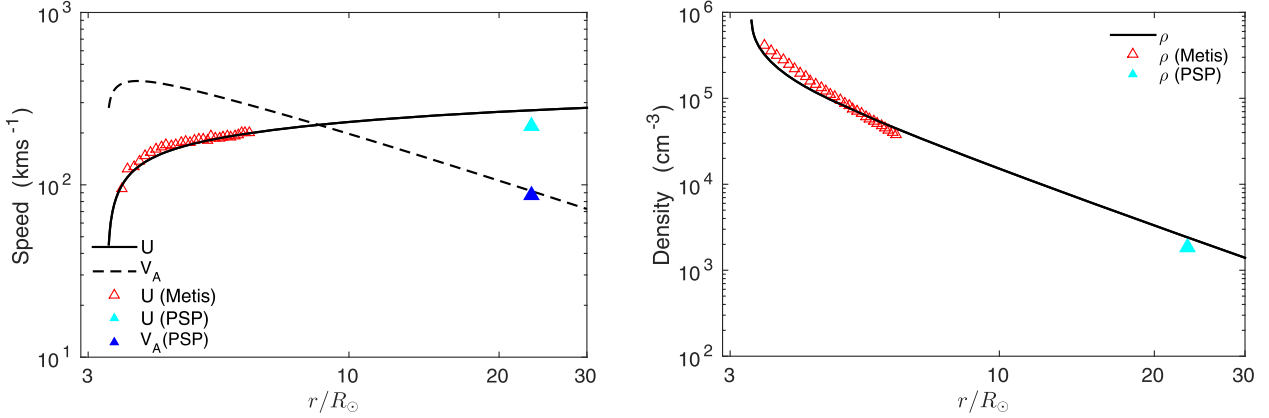


Figure 1. Comparison between the theoretical solar wind speed and Alfvén velocity (left), and the solar wind density (right) with the observed results of the plasma parcel measured by Metis/Solo (obtained from Telloni et al. 2022b) and PSP. The solid and dashed curves are the theoretical results. The open red triangles are the observed speed and density from Solo/Metis; the cyan full triangles are the observed speed and density; and the blue full triangle is the observed Alfvén speed measured by PSP during E7.

Zank et al. (2018a) argued that the magnetic carpet on the photosphere continuously pumps out the 2D structures along with a minority population of Alfvén waves (i.e., slab turbulence) above the photosphere. The 2D structures advect through the chromosphere, across the transition region, and into the solar corona. As advected 2D structures do not reflect at the transition region, there should be no abrupt and significant decrease in the 2D flux at the transition region, as is expected of outward-propagating Alfvén waves (Zank et al. 2018a). Zank et al. (2021) argued that the mechanism for heating the solar corona is the same for fast and slow solar wind flows. Recall that the slow solar wind studied in this letter emerges near the equatorial region and may be due to the liberation of hot loop material into open field regions by interchange reconnection above the photosphere (Fisk 2003). The slow solar wind in the equatorial region accelerates rapidly within $4 R_\odot$, similar to the fast solar wind in open field regions (Adhikari et al. 2020; Telloni et al. 2022a). Telloni et al. (2007) found observationally that the solar wind accelerates rapidly within $2-4 R_\odot$, consistent with Figure 1 (left). The Alfvén velocity increases initially to a peak value of $\sim 4 \times 10^2 \text{ km s}^{-1}$, decreases gradually, forming the Alfvén surface at $\sim 9.22 R_\odot$, and is similar to the in-situ PSP-observed Alfvén speed (blue full triangle).

Figure 2 presents the evolution of the basic turbulence quantities. As we see in Figure 2(a), the 2D outward Elsässer energy $\langle z^{\infty+2} \rangle$ (solid curve) is dissipated rapidly in the extended coronal region, after which it decreases more gradually. By contrast, the minority slab energy in outward-propagating modes $\langle z^+ \rangle$ (dashed curve) increases in the extended solar corona and decreases beyond the Alfvén surface. The initial increase in $\langle z^+ \rangle$ is due to the presence of the solar wind density gradient term, which acts as a source term. The heating of the solar corona by 2D turbulence is different from that due to counter-propagating Alfvén waves (Matthaeus et al. 1999; Verdini et al. 2010), which assumes that a large outward-propagating Alfvénic flux produces reflected Alfvén waves that interact nonlinearly to produce 2D modes that dissipate. In the NI MHD turbulence transport model, not only the slab component but also the 2D component reflect from the large-scale background inhomogeneity (see Equation (63) in Zank et al. 2017). Zank et al. showed that 2D Elsässer variables in an inhomogeneous plasma explicitly contain mixing and reflection terms, allowing the outward and inward 2D Elsässer variables to couple through the nonlinear terms and the large-scale field. The reflection and mixing terms were described by Zank

et al. (1996) as the mixing-expansion-compression-shear (MECS) tensor (Marsch & Tu 1989, 1990b, 1990a; Zhou & Matthaeus 1990a, 1990b; Zank et al. 1996). These are the terms responsible for generating inward/outward Elsässer fluctuations from outward/inward Elsässer fluctuations. This is similar to the reduced MHD model, where the 2D components reflect and produce the mixed cross helicities needed to generate the incompressible cascade (Einaudi et al. 1996; Dmitruk & Gómez 1999; Dmitruk et al. 2001; Dmitruk & Matthaeus 2003; Dmitruk et al. 2004; Perez & Chandran 2013). The theoretical $\langle z^+ \rangle$ is similar to PSP measurements and smaller than the theoretical $\langle z^{\infty+2} \rangle$. This can be understood by recognizing that the angle between the mean magnetic field and solar wind speed in the interval 18:40–20:40 UT is measured to be $\theta_{UB} \sim 165^\circ$, indicating that PSP measures the slab component, but not the 2D component. We can infer the properties of 2D and slab turbulence from PSP and Solo (and other spacecraft) from in-situ observations of magnetic and velocity fluctuations using the following criteria: (i) $65^\circ < \theta_{UB} < 115^\circ$, and (ii) $0^\circ < \theta_{UB} < 25^\circ$ (or $115^\circ < \theta_{UB} < 180^\circ$; Bieber et al. 1996; MacBride et al. 2008; Zank et al. 2020; Andrés et al. 2022; Adhikari et al. 2022). In case (i), the background fields are orthogonal and the observed wavevector is strictly perpendicular to the magnetic field. In case (ii), the background fields are parallel (or antiparallel) and the observed wavevector is strictly parallel to the magnetic field. The other wavevectors are present but cannot be observed by a single spacecraft. For other angles, all wavevectors can be observed, and so it is not possible to isolate parallel and perpendicular fluctuations in this way. The theoretical 2D + slab Elsässer energy (dashed-dotted curve) decreases gradually with increasing distance.

Figure 2(b) shows that the theoretical 2D fluctuating magnetic energy (solid curve) is larger than the theoretical slab component (dashed curve), and both decrease gradually with increasing distance. The theoretical $\langle B^2 \rangle$ is consistent with the PSP-observed $\langle B^2 \rangle$ for the reason given above. Similarly, the theoretical NI/slab fluctuating kinetic energy $\langle u^2 \rangle$ is consistent with that measured by PSP. The theoretical $\langle u^2 \rangle$ increases initially to a peak value and then decreases slowly. The theoretical $\langle u^{\infty 2} \rangle$ decreases rapidly, indicating that it is strongly dissipated.

In this model, the slab energy in backward-propagating modes $\langle z^* \rangle$ is 0, leading to a value of 1 for the slab normalized cross helicity σ_c^* (dashed curve in Figure 2(c)), and

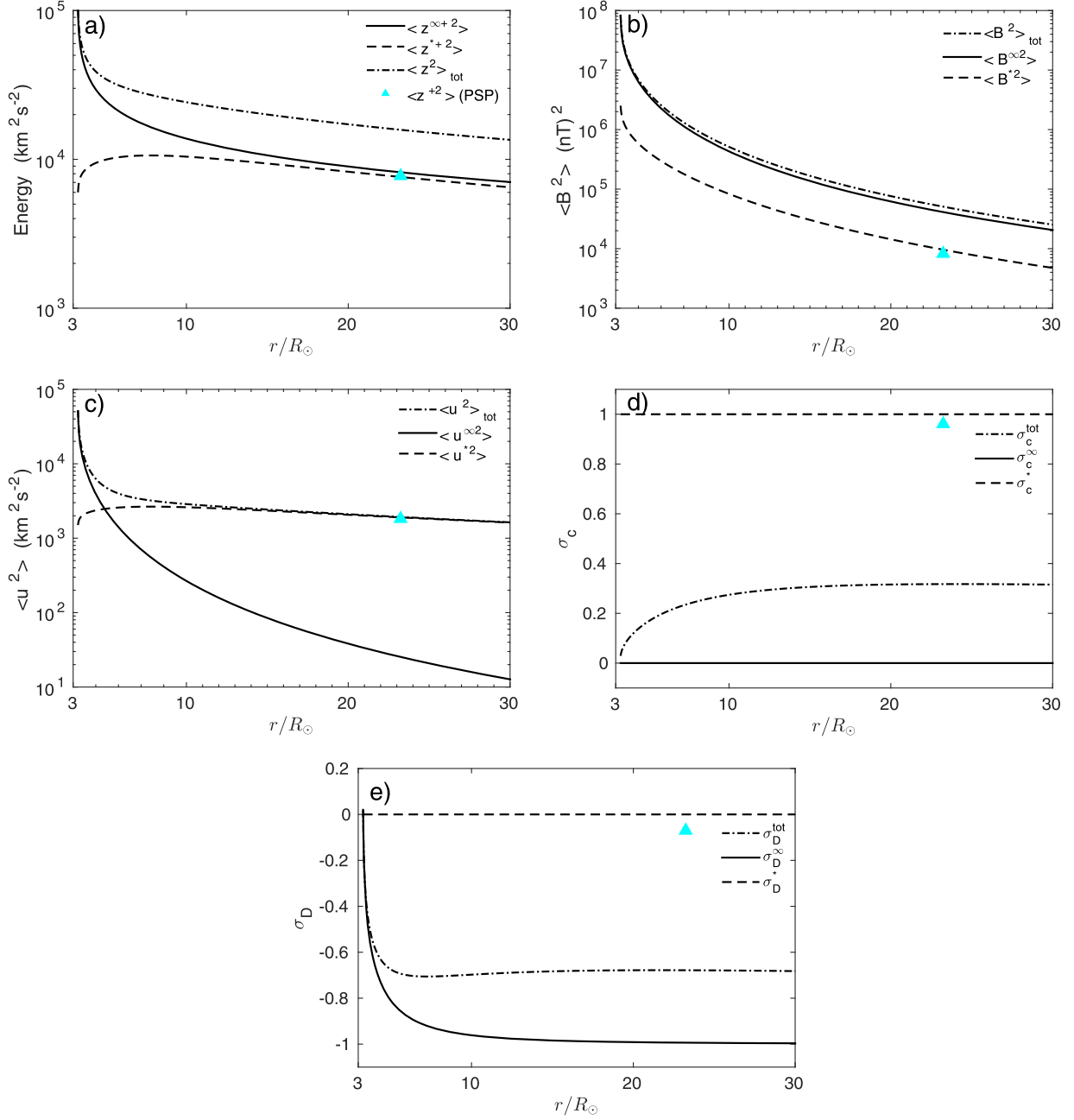


Figure 2. Radial evolution of the total (2D+slab), 2D, and slab turbulence energy from the extended coronal region to the very inner heliosphere. Panels (a), (b), (c), (d), and (e) describe the outward Elsässer energy, fluctuating magnetic energy, fluctuating kinetic energy, normalized cross helicity, and normalized residual energy, respectively. The solid curve represents the 2D component, the dashed curve the slab component, and the dashed-dotted curve the 2D+slab component. The cyan triangle denotes the corresponding PSP measurement.

is close to the observations. Note that the observed solar wind speed between 3.5 and $6.3 R_{\odot}$ ranges from 96 to 201 km s^{-1} , and that at $23.4 R_{\odot}$ is 219.34 km s^{-1} . This is an Alfvénic slow solar wind with a high cross-helicity value ($\sigma_c \sim 1$). As shown in Figure 2(a), the 2D outward and inward Elsässer energies are equal, leading to a zero 2D normalized cross helicity (solid curve in Figure 2(d)). The total normalized cross helicity (dashed-dotted curve) increases gradually until the Alfvén surface, and then remains approximately constant. Due to the assumption that the slab turbulent kinetic and magnetic energies are equipartitioned, the slab normalized residual energy (dashed curve) is zero as a function of distance, and is close to the observed value. The 2D normalized residual

energy (solid curve) decreases rapidly initially and then tends to -1 , i.e., the dominant 2D component is almost entirely composed of magnetic fluctuations.

The correlation length is an important parameter because it determines the turbulence heating rate (Adhikari et al. 2021a). Similar to the 2D outward and inward Elsässer energies, the corresponding 2D correlation lengths are equal (solid black and dashed curves in Figure 3(a)). The theoretical NI/slub correlation length for the energy in outward-propagating modes (dashed-dotted curve) increases with distance and is similar to PSP observations. The 2D correlation length of the magnetic field and velocity fluctuations (solid curves in Figures 3(b) and (c), respectively) increases much more rapidly than the

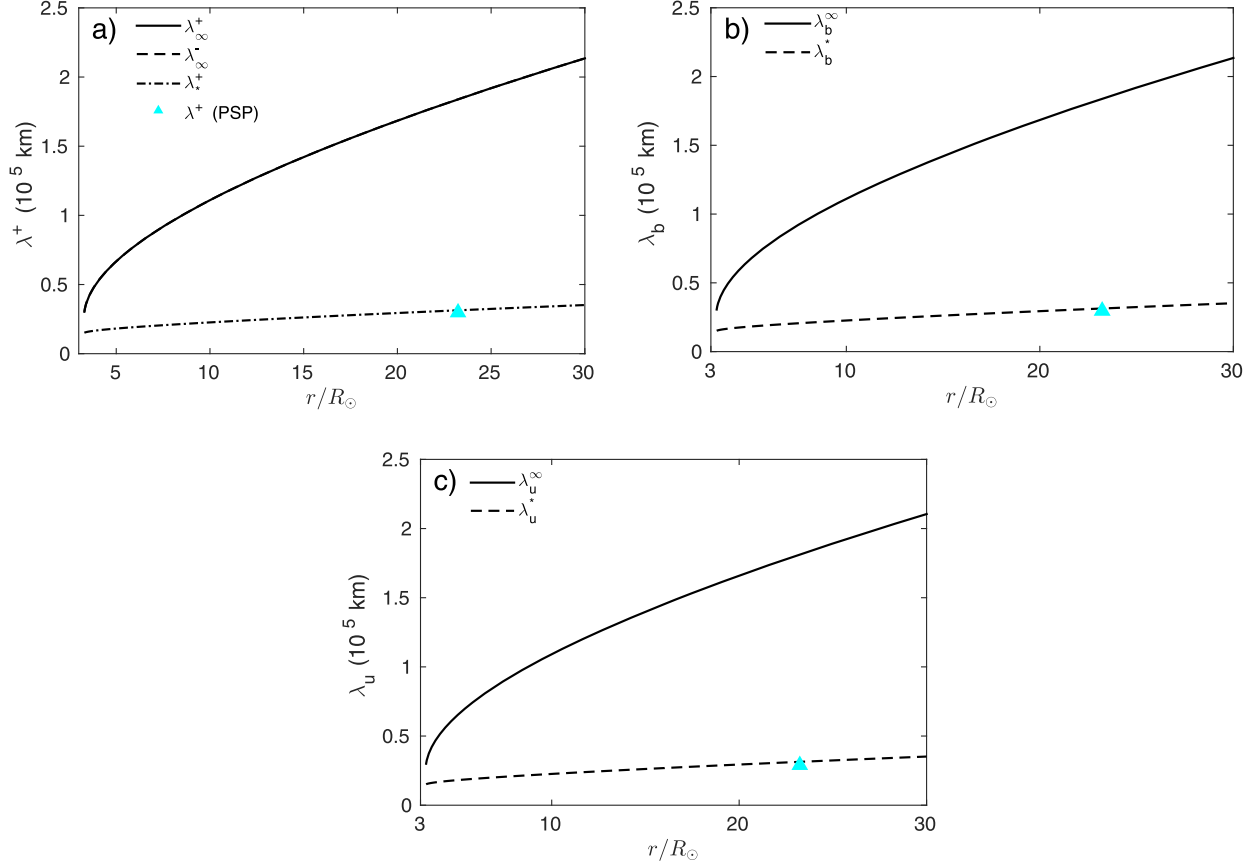


Figure 3. Radial evolution of the 2D (solid curve) and slab (dashed curve) (a) correlation lengths corresponding to the outward Elsässer energy, (b) fluctuating magnetic energy, (c) and fluctuating kinetic energy. The cyan triangle denotes the PSP measurements.

corresponding slab correlation lengths, the latter of which are in accordance with PSP measurements that can measure only the slab fluctuations as discussed above. This is different from Ruiz et al. (2011) and Cuesta et al. (2022). In their results, the slab (or parallel) correlation length increases faster than the 2D (or perpendicular) correlation length. However, they do not calculate the correlation length from the transverse fluctuations, as in Adhikari et al. (2022).

Figure 4 displays the turbulence pressure as a function of the heliocentric distance. The solid curve denotes the 2D turbulence pressure and the dashed curve the slab turbulence pressure. Initially, the 2D turbulence pressure is larger than the slab turbulence pressure; however, the former decreases more rapidly than the latter. The rapid decrease in the 2D turbulence pressure is due to the dominance of the 2D turbulent magnetic energy (see Figure 2(e)). The theoretical slab turbulence pressure is similar to that observed by PSP at $23.2 R_\odot$.

From a turbulence perspective, the dissipation of turbulence energy heats the coronal/solar wind plasma. The solar wind proton temperature is assumed to be 7×10^5 K at $3.3 R_\odot$, which increases to a peak value of $\sim 1.2 \times 10^6$ K and then decreases gradually but nonadiabatically in the expanding supersonic solar wind (Figure 5). The theoretical and PSP-observed proton temperature at $\sim 23 R_\odot$ are very similar.

5. Discussion and Conclusions

Telloni et al. (2022b) studied the PSP—SolO quadrature, combining remote imaging by the SolO Metis coronagraph and in-situ plasma data by PSP. We present a first comparison of

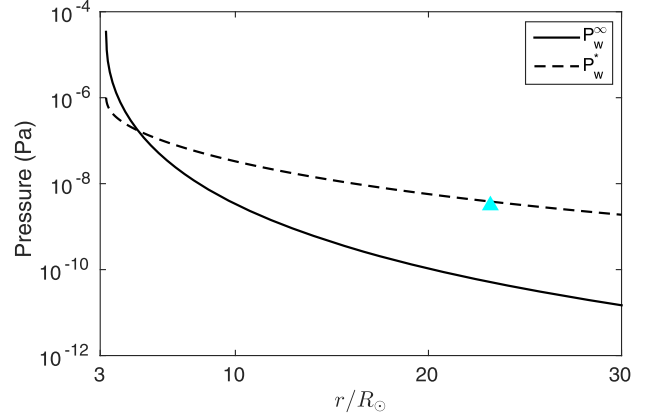


Figure 4. The 2D (solid curve) and slab (dashed curve) turbulence pressure as a function of the distance. The cyan triangle is the PSP-observed turbulence pressure.

the theoretical model and the joint PSP—SolO observations. We solved a solar wind + NI MHD turbulence model (Adhikari et al. 2020; Telloni et al. 2022a) from 3.3 to $30 R_\odot$, and compared (i) the theoretical solar wind speed and density with the corresponding remote observations from 3.5 to $6.3 R_\odot$ (Telloni et al. 2022b) and in-situ PSP measurements at $23.2 R_\odot$ or 0.11 au, and (ii) the theoretical turbulence energy and correlation length with PSP measurements. We used the PSP magnetometer and SPAN ion plasma data from 18:40–20:40 UT on 2021 January 18 (interval #1 in Telloni et al. 2022b) and calculated the transverse energy in the

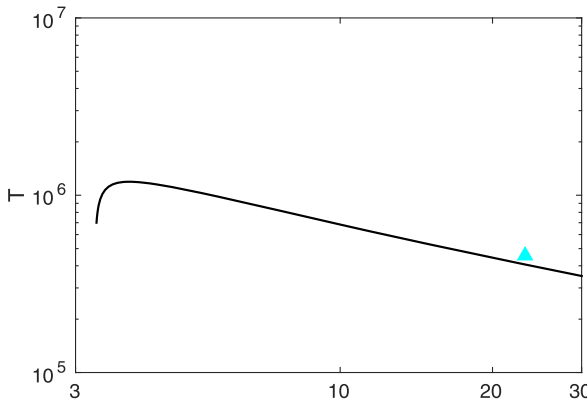


Figure 5. The solar wind proton temperature as a function of the distance. The cyan triangle is the PSP-observed proton temperature.

forward-propagating modes, fluctuating magnetic energy, fluctuating kinetic energy, normalized residual energy and cross helicity, and the corresponding correlation lengths using the method developed by Adhikari et al. (2022). We found that θ_{UB} , the angle between the mean solar wind flow and mean magnetic field for the selected interval is 165° , indicating that PSP observed primarily the slab turbulence component in this highly field-aligned flow. We found a very good agreement between theory and observations. We summarize our findings as follows:

1. The theoretical solar wind speed and density are consistent with those measured by SolO/Metis from $3.5\text{--}6.3 R_\odot$ and PSP at $23.2 R_\odot$. The theoretical and observed solar wind speed increases rapidly within $3.3\text{--}4 R_\odot$ ranging from 96 to 201 km s^{-1} , becoming supersonic at $\sim 5.16 R_\odot$. Thereafter, the theoretical solar wind speed increases gradually with distance and is consistent with the PSP speed of 219.34 km s^{-1} measured at $23.2 R_\odot$. PSP and Metis/SolO measured a slow solar wind stream emerging from the southern coronal hole near the equatorial region (Telloni et al. 2022b). The theoretical Alfvén velocity increases initially to a peak value $\sim 4 \times 10^2 \text{ km s}^{-1}$ and then decreases gradually to be consistent with that measured by PSP. In this model, the Alfvén surface is located at $\sim 9.22 R_\odot$.
2. The theoretical 2D outward Elsässer energy and fluctuating magnetic energy are larger than the corresponding slab components, the latter being close to the corresponding PSP-observed results. Similarly, the theoretical slab fluctuating kinetic energy is also consistent with the PSP-observed kinetic energy at $23.2 R_\odot$.
3. The theoretical slab normalized cross helicity is close to the PSP-observed cross helicity ($\sigma_c = 0.96$), indicating that PSP observed highly Alfvénic slow solar wind in the inner heliosphere (e.g., D'Amicis et al. 2019). The theoretical normalized slab residual energy is similar to the PSP-observed residual energy ($\sigma_D \sim -0.07$).
4. The theoretical 2D correlation lengths corresponding to outward Elsässer energy, and the magnetic field and velocity fluctuations exceed the theoretical slab correlation lengths; the slab correlation lengths are consistent with those observed by PSP.
5. We derived the two sets of equations in a conservation form, including superradial expansion, from the 2D + NI/slab turbulence transport equations that were derived

for the unidirectional Alfvén waves (Adhikari et al. 2020; Telloni et al. 2022a). Both sets of equations resemble the WKB form in the absence of a dissipation term, mixing term, and turbulence source (Wang et al. 2022). We calculated the theoretical 2D and slab turbulence pressures, and both decrease with increasing distance. The theoretical slab turbulence pressure is similar to that observed by PSP at $23.2 R_\odot$.

6. The proton temperature is assumed to be $7 \times 10^5 \text{ K}$ at $3.3 R_\odot$, increases to a maximum value of $\sim 1.2 \times 10^6 \text{ K}$, and then decreases gradually with the expanding solar wind. The PSP-measured temperature and the predicted temperature at $23.2 R_\odot$ are very similar.

Our theoretical results successfully describe the slow solar wind stream measured by Metis/SolO and PSP from the extended corona to the very inner heliosphere. Future combined studies using combined PSP, SolO, and BeliColombo measurements will be of great value.

We acknowledge the partial support of a Parker Solar Probe contract SV4-84017, an NSF EPSCoR RII-Track-1 cooperative agreement OIA-1655280, and NASA awards 80NSSC20K1783 and 80NSSC21K1319. The SWEAP Investigation and this study are supported by the PSP mission under NASA contract NNN06AA01C.

ORCID iDs

L. Adhikari <https://orcid.org/0000-0003-1549-5256>
 G. P. Zank <https://orcid.org/0000-0002-4642-6192>
 D. Telloni <https://orcid.org/0000-0002-6710-8142>
 L.-L. Zhao <https://orcid.org/0000-0002-4299-0490>

References

Adhikari, L., Zank, G. P., Bruno, R., et al. 2015, *ApJ*, **805**, 63
 Adhikari, L., Zank, G. P., & Zhao, L. 2021a, *Fluid*, **6**, 368
 Adhikari, L., Zank, G. P., Zhao, L. L., Nakanotani, M., & Tasnim, S. 2021b, *A&A*, **650**, A16
 Adhikari, L., Zank, G. P., & Zhao, L. L. 2020, *ApJ*, **901**, 14
 Adhikari, L., Zank, G. P., Zhao, L. L., & Telloni, D. 2022, *ApJ*, **933**, 56
 Andrés, N., Sahraoui, F., Huang, S., Hadid, L. Z., & Galtier, S. 2022, *A&A*, **661**, A116
 Antonucci, E., Romoli, M., Andretta, V., et al. 2020, *A&A*, **642**, A10
 Bale, S. D., Badman, S. T., Bonnell, J. W., et al. 2019, *Natur*, **576**, 237
 Bale, S. D., Goetz, K., Harvey, P. R., et al. 2016, *SSRV*, **204**, 49
 Bieber, J. W., Wanner, W., & Matthaeus, W. H. 1996, *JGR*, **101**, 2511
 Breech, B., Matthaeus, W. H., Cranmer, S. R., Kasper, J. C., & Oughton, S. 2009, *JGRA*, **114**, A09103
 Chandran, B. D. G., & Hollweg, J. V. 2009, *ApJ*, **707**, 1659
 Chhiber, R., Usmanov, A. V., Matthaeus, W. H., Parashar, T. N., & Goldstein, M. L. 2019, *ApJS*, **242**, 12
 Cranmer, S. R., Matthaeus, W. H., Breech, B. A., & Kasper, J. C. 2009, *ApJ*, **702**, 1604
 Cranmer, S. R., & van Ballegooijen, A. A. 2010, *ApJ*, **720**, 824
 Cranmer, S. R., van Ballegooijen, A. A., & Woolsey, L. N. 2013, *ApJ*, **767**, 125
 Cuesta, M. E., Chhiber, R., Roy, S., et al. 2022, *ApJL*, **932**, L11
 D'Amicis, R., Matteini, L., & Bruno, R. 2019, *MNRAS*, **483**, 4665
 Dmitruk, P., & Gómez, D. O. 1999, *ApJL*, **527**, L63
 Dmitruk, P., & Matthaeus, W. H. 2003, *ApJ*, **597**, 1097
 Dmitruk, P., Matthaeus, W. H., & Lanzerotti, L. J. 2004, *GeoRL*, **31**, L21805
 Dmitruk, P., Milano, L. J., & Matthaeus, W. H. 2001, *ApJ*, **548**, 482
 Einaudi, G., Velli, M., Politano, H., & Pouquet, A. 1996, *ApJL*, **457**, L113
 Engelbrecht, N. E., & Strauss, R. D. T. 2018, *ApJ*, **856**, 159
 Fisk, L. A. 2003, *JGRA*, **108**, 1157
 Fisk, L. A., Schwadron, N. A., & Zurbuchen, T. H. 1999, *JGR*, **104**, 19765
 Holzer, T. E., & Axford, W. I. 1970, *ARA&A*, **8**, 31
 Horbury, T. S., O'Brien, H., Carrasco Blazquez, I., et al. 2020, *A&A*, **642**, A9

Kasper, J. C., Abiad, R., Austin, G., et al. 2016, *SSRv*, **204**, 131

Kopp, R. A., & Holzer, T. E. 1976, *SoPh*, **49**, 43

Landau, L. D., & Lifshitz, E. M. 1987, *Fluid Mechanics* (2nd ed.; Oxford: Pergamon)

Leer, E., Holzer, T. E., & Fla, T. 1982, *SSRv*, **33**, 161

MacBride, B. T., Smith, C. W., & Forman, M. A. 2008, *ApJ*, **679**, 1644

Marsch, E., & Tu, C.-Y. 1989, *JPlPh*, **41**, 479

Marsch, E., & Tu, C.-Y. 1990a, *JGR*, **95**, 8211

Marsch, E., & Tu, C.-Y. 1990b, *JGR*, **95**, 11945

Matthaeus, W. H., Oughton, S., Pontius, D. H., Jr., & Zhou, Y. 1994, *JGR*, **99**, 19267

Matthaeus, W. H., Zank, G. P., Oughton, S., Mullan, D. J., & Dmitruk, P. 1999, *ApJL*, **523**, L93

McKenzie, J. F., Banaszkiewicz, M., & Axford, W. I. 1995, *A&A*, **303**, L45

Moses, J. D., Antonucci, E., Newmark, J., et al. 2020, *NatAs*, **4**, 1134

Noci, G., Kohl, J. L., & Withbroe, G. L. 1987, *ApJ*, **315**, 706

Owen, C. J., Bruno, R., Livi, S., et al. 2020, *A&A*, **642**, A16

Panasenco, O., Velli, M., D'Amicis, R., et al. 2020, *ApJS*, **246**, 54

Perez, J. C., & Chandran, B. D. G. 2013, *ApJ*, **776**, 124

Ruiz, M. E., Dasso, S., Matthaeus, W. H., Marsch, E., & Weygand, J. M. 2011, *JGRA*, **116**, A10102

Telloni, D., Adhikari, L., Zank, G. P., et al. 2022a, *ApJ*, **929**, 98

Telloni, D., Zank, G. P., Sorriso-Valvo, L., et al. 2022b, *ApJ*, **935**, 112

Telloni, D., Andretta, V., Antonucci, E., et al. 2021, *ApJL*, **920**, L14

Telloni, D., Antonucci, E., & Dodero, M. A. 2007, *A&A*, **476**, 1341

van de Hulst, H. C. 1950, *BAN*, **11**, 150

Verdini, A., Velli, M., Matthaeus, W. H., Oughton, S., & Dmitruk, P. 2010, *ApJL*, **708**, L116

von Karman, T., & Howarth, L. 1938, *RSPSA*, **164**, 192

Wan, M., Oughton, S., Servidio, S., & Matthaeus, W. H. 2012, *JFM*, **697**, 296

Wang, B. B., Zank, G. P., Adhikari, L., & Zhao, L. L. 2022, *ApJ*, **928**, 176

Withbroe, G. L. 1988, *ApJ*, **325**, 442

Zank, G. P., Adhikari, L., Hunana, P., et al. 2017, *ApJ*, **835**, 147

Zank, G. P., Adhikari, L., Hunana, P., et al. 2018a, *ApJ*, **854**, 32

Zank, G. P., Adhikari, L., Zhao, L. L., et al. 2018b, *ApJ*, **869**, 23

Zank, G. P., Dosch, A., Hunana, P., et al. 2012, *ApJ*, **745**, 35

Zank, G. P., Matthaeus, W. H., & Smith, C. W. 1996, *JGR*, **101**, 17093

Zank, G. P., Nakamoto, M., Zhao, L. L., Adhikari, L., & Telloni, D. 2020, *ApJ*, **900**, 115

Zank, G. P., Zhao, L. L., Adhikari, L., et al. 2021, *PhPl*, **28**, 080501

Zhou, Y., & Matthaeus, W. H. 1990a, *JGR*, **95**, 14881

Zhou, Y., & Matthaeus, W. H. 1990b, *JGR*, **95**, 14863

Zhou, Y., & Matthaeus, W. H. 1990c, *JGR*, **95**, 10291